RSC Advances

PAPER

View Article Online
View Journal | View Issue

Cite this: *RSC Adv.*, 2026, **16**, 22062

Efficient removal of methylene blue dye using magnetized titanate nanotubes

Rania N. Zohny, Ayman H. Zaki,* A. A. Farghali and Mohamed Taha

This study investigates the removal of methylene blue (MB) dye, a model organic pollutant, using sodium titanate nanotubes (Na/TNTs) and magnetized titanate nanotubes (Mag/TNTs) as efficient nano-adsorbent materials. Mag/TNTs consist of cobalt ferrite ($CoFe_2O_4$) nanoparticles supported on Na/TNTs. Both adsorbents were synthesized *via* a simple hydrothermal method and characterized using SEM, HRTEM, XRD, BET, zeta potential analysis, and FT-IR techniques. Multiwalled open-ended nanotubes were formed, as demonstrated by TEM images. Their typical lengths ranged from 100 to 150 nm, and their average outer diameters were 12.46 and 12.88 nm for Na/TNTs and Mag/TNTs, respectively. Batch adsorption experiments were conducted to evaluate the effects of pH, adsorbent dose, initial dye concentration, temperature, contact time, and adsorbent regeneration on the removal efficiency of MB dye. Among five isotherm models (Langmuir, Freundlich, Langmuir–Freundlich, Sips, Dubinin–Radushkevich), Langmuir–Freundlich and Sips provided the best fits, indicating heterogeneous surface adsorption. Kinetic data were best described by pseudo-second-order and mixed 1,2-order models among the four tested models (pseudo-first-order, pseudo-second-order, mixed 1,2-order, Avrami), suggesting combined physisorption and chemisorption. The maximum adsorption capacities for Na/TNTs and Mag/TNTs increased with temperature, reaching 178.98 mg g^{-1} and 180.50 mg g^{-1} at 328 K, respectively. Thermodynamic parameters confirmed that the process is spontaneous and exothermic. Monte Carlo simulations revealed that while $CoFe_2O_4$ exhibits stronger individual interactions with MB, the higher surface area of Na/TNTs leads to greater overall removal. The study demonstrates that Mag/TNTs are efficient, separable (using an external magnet), and reusable adsorbents for cationic dye removal from wastewater.

Received 18th March 2026
Accepted 14th April 2026

DOI: 10.1039/d6ra02268e

rsc.li/rsc-advances

1. Introduction

Clean water resources and their sustainability have been considered one of the most important global issues over the centuries. Freshwater quality enhancement has received great attention from researchers worldwide.[1] Urbanization, over-population, and human activities such as industrialization and agriculture have side effects on clean water resources.[2] Water pollution arises from the discharge of industrial, agricultural, urban, and domestic effluents into water.[3] The existence of these pollutants causes several diseases such as dysentery, diarrhea, hepatitis A, and cholera. It is speculated that more than 842 000 people die from diarrhea around the world.[4]

Organic dyes are serious pollutants in wastewater, and cause a threat to the aquatic environment through the prevention of light transfer to the aquatic life in water, and consequently hinder the photosynthetic process.[5] Every year, thousands of tons of dyes are produced, with global production estimated at approximately 7×10^5 tons.[6,7] Methylene blue (MB) is one of the most common cationic dyes, widely used for dyeing leathers, food, pharmaceuticals, cosmetics,[8] papers, and fabrics, and is discharged as effluents into surface and groundwater.[9] Several risks to human health come from MB presence in water, such as tissue necrosis, vomiting, cyanosis, jaundice, Heinz body formation, increased heart beat rate, shock, *etc.*[10] Several methods have been proposed for removing the organic contaminants from water. These methods include adsorption, ion exchange, advanced oxidation processes, photochemical treatments, and biological treatment methods.[7] One of the primary and advantageous methods for dye removal is the adsorption process, as it has a simple design, low cost, high efficiency, and avoids the generation of toxic materials.[2,11,12] Numerous adsorbent materials that have been investigated, such as carbon nanotubes,[13] hydroxyapatite nanoparticles,[14] zinc oxide nanoparticles,[15] titanium dioxide nanoparticles,[16] cobalt zinc ferrite nanoparticles,[17] and titanate nanotubes (TNTs). These adsorbents are characterized by several properties such as high surface area, ion-exchange ability, high stability, large pore volume, and surface functionalized with hydroxyl (OH) groups.[2,18,19] The ion-exchange capability of

Material Science and Nanotechnology Department, Faculty of Postgraduate Studies for Advanced Sciences, Beni-Suef University, Beni-Suef, Egypt. E-mail: ayman.zaki@psas.bsu.edu.eg

titanate nanotubes enables efficient removal of cationic dyes from wastewater.[2] However, the separation of TNTs after water treatment remains a great challenge. Modifying TNTs with magnetic materials will overcome this challenge, as they can be easily separated from wastewater using an external magnet and could be easily reused for many treatment cycles.

$CoFe_2O_4$ is a promising magnetic adsorbent for dye removal from wastewater due to its good chemical and thermal stability, a simple chemical composition, and high magnetic properties at the nanoscale.[20,21] The spinel structure of $CoFe_2O_4$ provides numerous surface-active sites that enhance the adsorption of water pollutants.[22] Moreover, the magnetic properties of $CoFe_2O_4$ enable rapid separation using an external magnetic field.[23]

This work aims to combine the advantages of titanate nanotubes as an excellent adsorbent for dye removal with the good magnetic properties of $CoFe_2O_4$.[24,25] In this regard, we have fabricated Na/TNTs and Mag/TNTs and tested their ability for efficient MB removal from water under various conditions. Furthermore, the adsorption mechanism was investigated using Monte Carlo (MC) simulation to provide molecular-level insights into the interactions between MB molecules and the adsorbent surfaces.

2. Materials and methods

2.1. Materials

All chemicals were of analytical grade and used as received without any further purification. Sodium hydroxide (NaOH) was purchased from PioChem laboratory reagents (Kenya, packed in Egypt), and anatase TiO_2 powder was obtained from Loba Chemie laboratory reagents (India). Cobalt sulfate ($CoSO_4$), ferric nitrate ($Fe(NO_3)_3$), and MB powder were purchased from Oxford Laboratory Reagents (India) and Central Drug House Ltd (India), respectively.

2.2. Synthesis of Na/TNTs and Mag/TNTs

2.2.1. Preparation of Na/TNTs. Na/TNTs were synthesized by the hydrothermal method.[2] Approximately 50 g of TiO_2 was added to 125 mL of 10 M NaOH, then stirred for 1 h until forming a white suspension, followed by hydrothermal treatment in a Teflon-lined stainless-steel autoclave at 160 °C for 23 h. Eventually, the white precipitate was washed and dried in the oven at 80 °C overnight.

2.2.2. Preparation of Mag/TNTs. 20 mL of an aqueous solution containing 0.38 g of $CoSO_4$ and 1.2 grams of $Fe(NO_3)_3$ was mixed with 60 mL of an aqueous solution containing 2 g of TiO_2.[26] The mixture was stirred for 1 h, and the pH of the mixture was adjusted to 12 using NaOH. Afterward, this mixture was transferred to a Teflon-lined stainless-steel autoclave at 180 °C for 24 h. The formed precipitate was mixed with 80 mL of NaOH (10 mol L^{-1}) and stirred for 2 h, then this suspension was transferred to a Teflon-lined stainless-steel autoclave and placed in oven at 150 °C for an additional 24 h. Finally, the obtained dark precipitation was washed with distilled water, followed by centrifugation several times. The dark powder was dried at 80 °C overnight and kept at room temperature until used.

2.3. Batch adsorption of MB

The adsorption performance of Na/TNTs and Mag/TNTs for MB was investigated through different adsorption parameters. 40 mL of MB dye solution was shaken and tested under different parameters such as (i) pH (3 to 12), (ii) initial dye concentration (5 ppm to 320 ppm), (iii) adsorbent dose (20 mg to 160 mg), temperature (298 K to 328 K), and (iv) time (10 min to 210 min). For kinetic studies, samples were withdrawn from the solution at regular intervals and centrifuged at 4000 rpm for 3 min to separate the adsorbent. For adsorption isotherm studies, different initial concentrations of MB were contacted with a fixed amount of adsorbent and stirred for a certain time. After equilibrium was reached, the samples were centrifuged at 4000 rpm for 3 min, and the supernatant was collected for concentration analysis. A UV-visible spectrophotometer (Alpha-1900S) was used to measure the concentration of MB dye in the supernatant at a wavelength of 664 nm. It is worth mentioning that every adsorption experiment was carried out in triplets. The equilibrium adsorption capacity (q_e, mg g^{-1}) (eqn (1)) and removal efficiency (% R) (eqn (2)) of MB by Na/TNTs and Mag/TNTs were calculated as:

$$q_e = \frac{(C_0 - C_e)}{W} \times V \quad (1)$$

$$\% R = \frac{(C_0 - C_e)}{C_0} \times 100 \quad (2)$$

where C_0 and C_e are the initial and equilibrium MB concentration (mg L^{-1}), respectively. V (L) is the volume of the MB aqueous solution. W (g) is the mass of the adsorbent material.

2.3.1. Effect of pH on the adsorption of MB by Na/TNTs and Mag/TNTs. pH of the solution significantly influences the adsorption process of methylene blue dye because of the alteration in the adsorbent's surface charge with the change of pH of the solution.[2] To study the effect of pH, 10 mg of the adsorbent material was used to remove MB (40 ppm, 40 mL) by shaking the samples for 1 h. pH was studied at (3, 5, 7, 9, and 12) at room temperature.

2.3.2. Effect of adsorbent dose on MB removal. A sorbent dose ranging from 20 to 160 mg was employed for the removal of MB (400 ppm, 40 mL) at pH 5, with continuous shaking for 1 h.

2.3.3. Effect of contact time. To investigate the effect of contact time, aliquots were withdrawn at 3 min intervals from the MB solution (140 ppm, 40 mL; pH 5) containing 40 mg of adsorbent over a total contact time of 10–210 min.

2.3.4. Effect of initial MB concentration and temperature. To study the effect of dye concentration and temperature on MB adsorption, 20 mg of the adsorbent material was used with an initial dye concentration (5 ppm to 320 ppm) at pH 5 and shaking overnight at different temperatures (298, 308, 318, 328) K.

2.3.5. Zeta potential measurement. Surface charge properties of Na/TNTs and Mag/TNTs were measured using the

Zetasizer Nano instrument (Malvern Instruments, UK) at room temperature. 1 mg of each sample was dispersed in 1 mL of deionized water, then ultrasonicated for 15 min to achieve uniform dispersion. pH of the solution was adjusted to 3,5,7,9, and 12 using HCl or NaOH solutions.

2.3.6. Reusability experiment. The reusability of the adsorbent materials reduces the overall cost of the adsorption process.[27,28] After each adsorption experiment, the adsorbent was separated by centrifugation and washed several times with distilled water and ethanol under water-bath sonication to desorb MB. The material was then dried at 80 °C overnight. This procedure was repeated under the same conditions for five consecutive cycles to evaluate the reusability of Na/TNTs and Mag/TNTs.

2.4. MC simulation

In this study, the BIOVIA Materials Studio 2020 package [https://www.3ds.com] was used to investigate the adsorption mechanism of MB on $Na_2Ti_3O_7$ and $CoFe_2O_4$ surfaces *via* MC simulation. The crystal structures of $Na_2Ti_3O_7$ and $CoFe_2O_4$ were obtained from the open-access Materials Project database.[29] The Bravais lattice of $Na_2Ti_3O_7$ is triclinic, with lattice parameters $a = 8.546$ Å, $b = 3.792$ Å, and $c = 9.137$ Å, and lattice angles $\alpha = 90°$, $\beta = 101.88°$, and $\gamma = 90°$. $CoFe_2O_4$ exhibits a cubic structure, with all angles equal to 90° and a lattice constant of $a = 8.446$ Å. Using the Forcite module in Materials Studio, geometry optimization of the MB molecule, $Na_2Ti_3O_7$, and $CoFe_2O_4$ was carried out before performing the MC simulations. Compass III force[30] with its charges is used in all calculations. An atom-based summation method was employed to calculate both electrostatic and van der Waals interactions during the dye geometry optimization. A cubic-spline truncation scheme was applied, using a cutoff distance of 18.5 Å, a spline width of 1 Å, and a buffer width of 2 Å. For $Na_2Ti_3O_7$, and $CoFe_2O_4$ optimizations, the electrostatic interactions were treated using the Ewald summation, whereas the van der Waals interactions were computed using an atom-based method. In this atom-based scheme, the same cubic-spline truncation parameters used for MB optimization were applied. For the electrostatic summation, an Ewald accuracy of 1.0×10^{-5} kcal mol^{-1} and a 2 Å buffer width were used. The geometry optimization was considered converged when the energy change, maximum force, and atomic displacement decreased to less than 1.0×10^{-4} kcal mol^{-1}, 0.005 kcal mol^{-1}·Å^{-1}, and 5.0×10^{-5} Å, respectively. In the case of unit-cell optimizations, these convergence criteria were applied together with a stress tolerance of 0.001 GPa and an external pressure of 0 GPa. The smart optimization algorithm is employed in all optimization processes. The optimized lattice parameters of $Na_2Ti_3O_7$ were $a = 8.269$ Å (3.2% deviation), $b = 3.744$ Å (1.3% deviation), and $c = 8.865$ Å (3.0% deviation), with lattice angles $\alpha = 90°$, $\beta = 103.05°$ (1.1% deviation), and $\gamma = 90°$. The optimized lattice parameters of $CoFe_2O_4$ retained a cubic structure, with all angles equal to 90° (0% deviation) and a lattice constant of $a = 9.418$ Å (11.5% deviation). The small deviations between the optimized and experimental lattice parameters demonstrate the reliability of the COMPASS forcefield for $Na_2Ti_3O_7$ and $CoFe_2O_4$. This validation supports its use in subsequent MC simulations to explore the adsorption mechanism, despite the slightly higher deviation in $CoFe_2O_4$. This forcefield was chosen for its broad parameterization, enabling accurate modeling of hybrid inorganic–organic systems. Mainly, it provides reliable representations of metal oxides and aromatic organic molecules. COMPASS III force field effectively described the associated metal–π interactions through its optimized van der Waals and electrostatic potential terms.[28,31] Forcefield atom types assigned to the constituent atoms of $Na_2Ti_3O_7$, $CoFe_2O_4$, and MB dye are mentioned in Table S1 (SI). Supercells of $Na_2Ti_3O_7$ (45.499 × 45.68 × 76.167 Å) and $CoFe_2O_4$ (41.378 × 41.807 × 59.714 Å) were generated. The $Na_2Ti_3O_7$ (1 0 0) and $CoFe_2O_4$ (3 1 1) surfaces were constructed with 50 Å vacuum layers to prevent interlayer interactions. In all MC simulations, non-bonded interactions were treated using the same summation methods applied during the optimization of $Na_2Ti_3O_7$ and $CoFe_2O_4$. The Adsorption Locator module was employed to perform simulated annealing within the canonical ensemble using the Metropolis MC method. The parameters for the simulated annealing process were as follows: five heating cycles of 50 000 steps each. Simulated annealing MC simulation was conducted with a maximum temperature of 1.0×10^5 K to enable broad configurational sampling, followed by cooling to 100 K (final temperature) to achieve the lowest-energy adsorption configuration.[2,28,32,33] This approach helps identify the lowest-energy configuration of dye molecules on $Na_2Ti_3O_7$ and $CoFe_2O_4$ surfaces, from which the corresponding adsorption energies (ΔE_{ads}) were calculated (eqn (3)).[34] During the simulations, the $Na_2Ti_3O_7$ and $CoFe_2O_4$ surfaces were kept fixed, and their energies were defined as zero reference points. The ΔE_{ads} was calculated as the total energy change associated with the adsorption of the relaxed dye on the $Na_2Ti_3O_7$ and $CoFe_2O_4$ surfaces. It is defined as the sum of the rigid adsorption energy (ΔE_{rigid}), which corresponds to the energy change when the unrelaxed adsorbate initially adsorbs on the substrate, and the deformation energy ($\Delta E_{deformation}$), which is the energy released (or required) as the adsorbate relaxes on the surface.

$$\Delta E_{ads} = \Delta E_{rigid} + \Delta E_{deformation}, \quad (3)$$

This definition clarifies the contributions of both initial adsorption and subsequent structural relaxation of the adsorbate. The Cartesian coordinates of the optimized dye-surface configurations are provided in the supporting information, including the lowest-energy geometries. Different configurational move types were assigned to each species during the MC simulation. A conformer (0.32 probability), translation (0.32 probability), rotation (0.32 probability), and regrowth (0.03 probability) move ratio of 1 was applied to the MB dye molecules to fully sample their positional changes.[35,36] In contrast, chloride ions were restricted to translational moves only, consistent with their spherical geometry. After five annealing cycles (5 × 50 000 steps), both the total energy and adsorption configuration stop changing and reach a stable state, confirming convergence. Increasing the number of simulation cycles

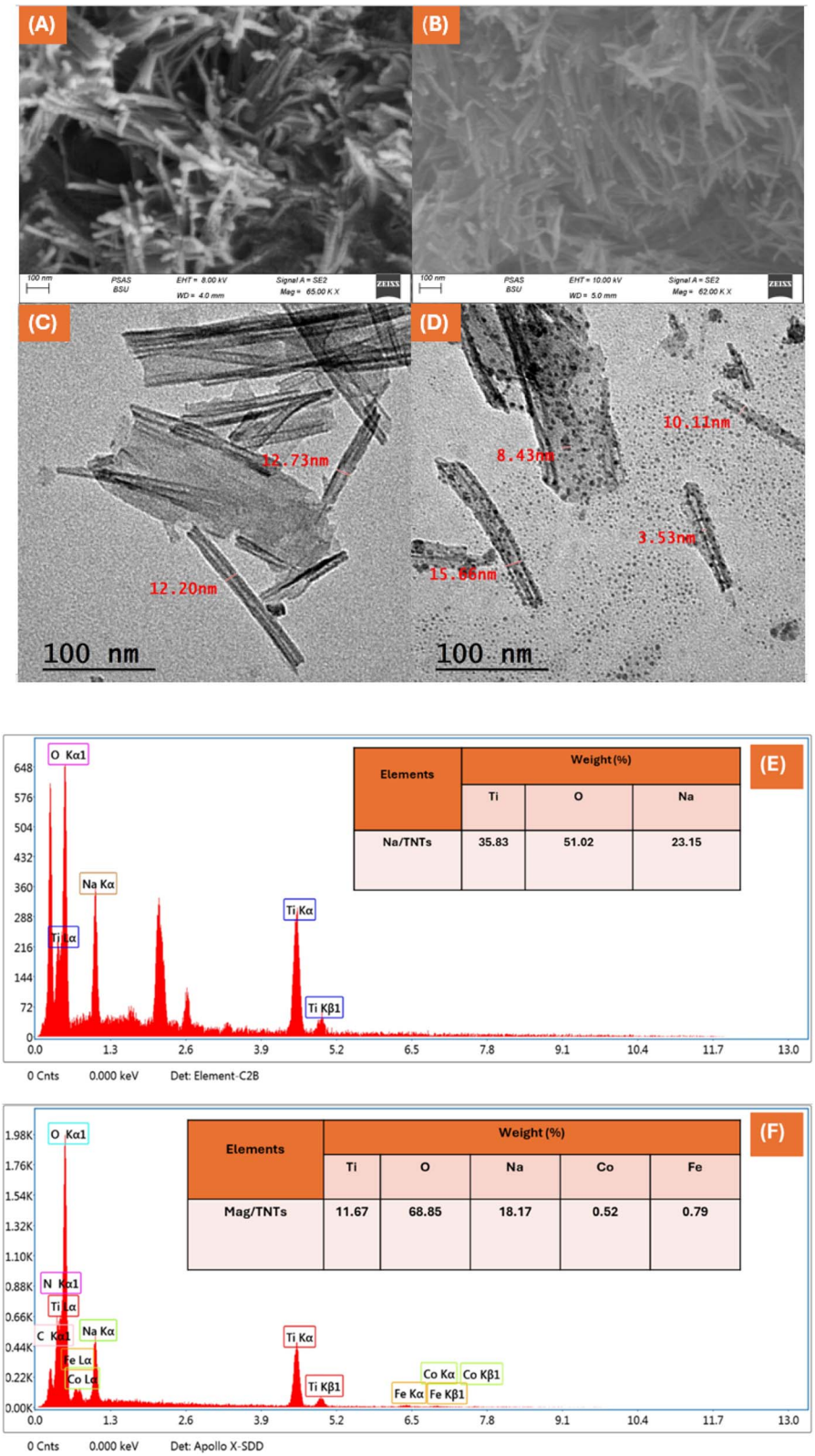

Fig. 1 SEM, TEM images, and EDX for Na/TNTs (A, C and E), Mag/TNTs (B, D and F), respectively.

produced no significant change in the lowest-energy configuration or adsorption energy.

3. Results and characterization

3.1. Characterization of Na/TNTs and Mag/TNTs

Fig. 1A–D shows high-resolution SEM (Zeiss Sigma 500 VP Analytical FESEM, Carl Zeiss, Germany) and TEM (JEM-1230 (600Kx)) of Na/TNTs and Mag/TNTs, both with a uniform tubular structure. These images proved the successful formation of nanotubes. TEM images showed multiwalled open-ended nanotubes with an average length between 100 nm and 150 nm for both, and average outer diameters of 12.46 nm and 12.88 nm for Na/TNTs and Mag/TNTs, respectively. The spherical particles that spread over the nanotubes indicate the presence of $CoFe_2O_4$ in the prepared material.[24,37] EDX analysis investigated the elemental composition of the prepared Na/TNTs and Mag/TNTs. The analysis detected the presence of Ti, O, and Na, which are the components of Na/TNTs (Fig. 1E) with weight percentages (35.83, 51.02, and 23.15) wt%, respectively, and the presence of Ti, O, Na, Co, and Fe which are the main components of Mag/TNTs (Fig. 1F) with weight percentages (11.67, 68.85, 18.17, 0.52, and 0.79) wt%, respectively.

The crystalline structure of Na/TNTs and Mag/TNTs was examined using XRD (Malvern PANalytical Empyrean 3 diffractometer). Fig. 2 shows the XRD patterns of Na/TNTs and Mag/TNTs. The four reflections at 2θ values of 9.27°, 24.41°, 28.17°, and 48.29° confirm the successful preparation of Na/TNTs.[38] The formation of Na/TNTs is verified according to the ICDD (International Center for Diffraction Data) card no. 00-059-0666.[39] XRD peak at $2\theta = 9.27°$ refers to the interlayer spacing of the layered Na/TNTs structure. After magnetization, the XRD pattern of Mag/TNTs retains the characteristic titanate peak and exhibits additional diffraction peaks attributed to the crystalline $CoFe_2O_4$ phase. The new peaks appear at (35.6°, 57.2°, 62.8°), corresponding to magnetic $CoFe_2O_4$, matching the ICDD card no. 22-1086.[24]

The surface functional groups of Na/TNTs and Mag/TNTs were identified by Fourier transform infrared (FTIR) spectroscopy (Bruker Vertex 70 spectrometer). The broad peak at 3388.01 cm^{-1} represents the O–H stretching vibration of surface hydroxyl groups and adsorbed water molecules. Also, the H–O–H bending vibration appears with strong absorption at 1625.81 cm^{-1}, confirming the existence of water molecules in the titanate nanotubes. The spectrum of Na/TNTs (Fig. 3a) shows a characteristic peak of Ti–O stretching vibration at 915.62 cm^{-1},[40] as well as an absorption peak appearing at 463.89 cm^{-1}, referring to the Ti–O–Ti crystal phonons.[2] As shown in Fig. 3b, the band observed at 451 cm^{-1} refers to the presence of Co–Fe vibration.[24]

The BET results revealed that the surface area reached 138.1 $m^2\ g^{-1}$ and 96.253 $m^2\ g^{-1}$, with total pore volume of 0.2238 $cm^3\ g^{-1}$ and 0.2762 $cm^3\ g^{-1}$ at an adsorption temperature of 77 K for both Na/TNTs and Mag/TNTs, respectively. In the adsorption isotherm (Fig. 4a), both Na/TNTs and Mag/TNTs showed a gradual increase in nitrogen quantity at P/P_0 near zero, with a rapid increase at high relative pressure ($P/P_0 > 0.8$). The results indicated that Na/TNTs exhibited a higher surface area and a small pore volume, whereas Mag/TNTs exhibited a lower surface area and a large pore volume. Pore size distribution plays a role in determining how much the nitrogen adsorption uptake contributes to surface area and pore volume. In the case of Na/TNTs, there are many narrow mesopores, which lead to a large internal surface area of 138.1 $m^2\ g^{-1}$ with an overall small pore volume of 0.2238 $cm^3\ g^{-1}$. Resulting in a high quantity of nitrogen adsorbed close to P_0 for Na/TNTs. On the

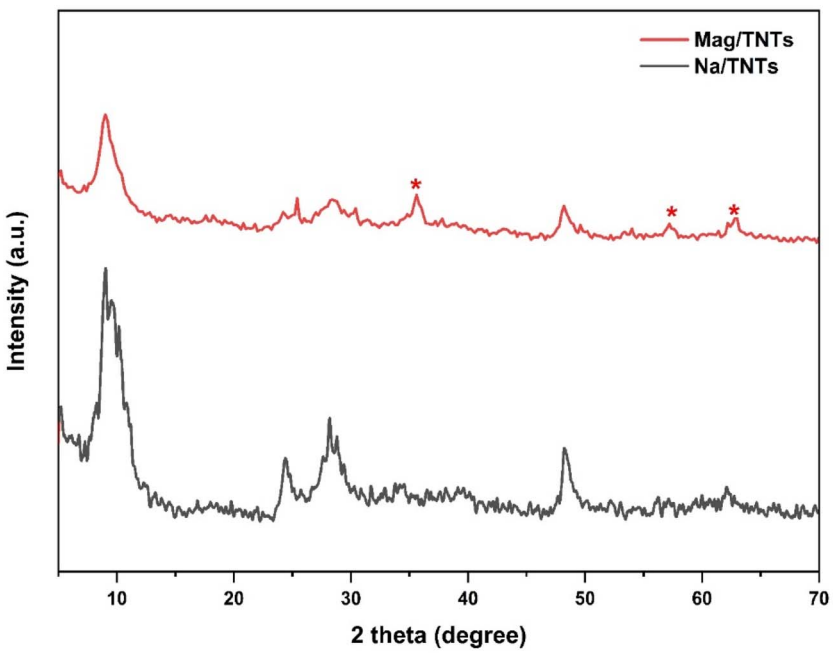

Fig. 2 XRD pattern of Na/TNTs and Mag/TNTs.

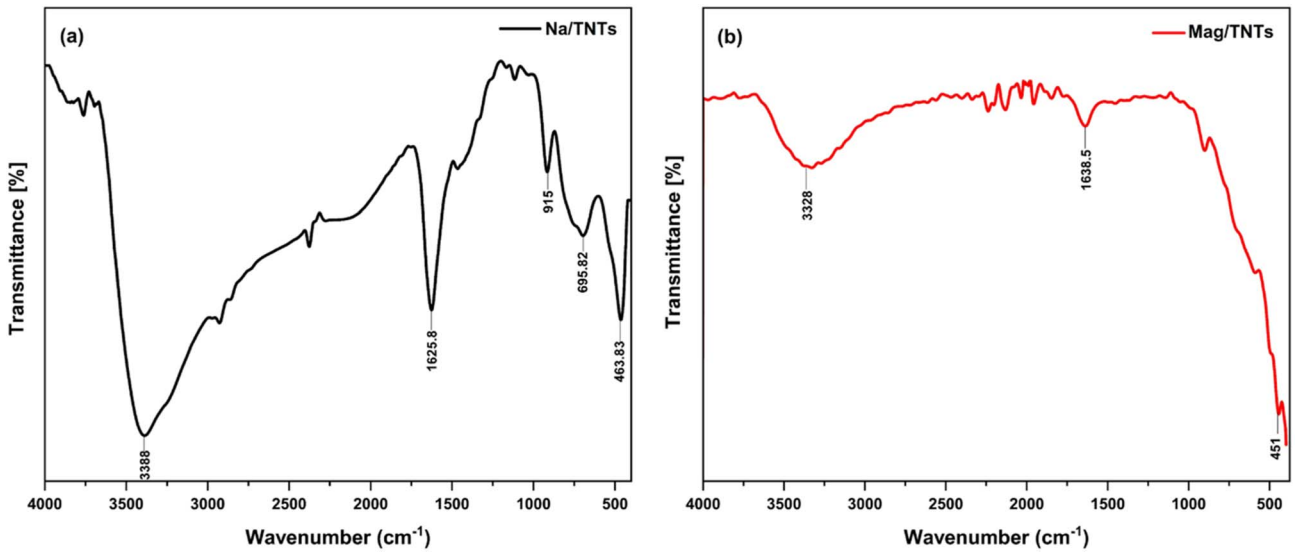

Fig. 3 FTIR spectrum of Na/TNTs (a) and Mag/TNTs (b).

contrary, Mag/TNTs have wider mesopores that provide a larger pore volume (0.2762 $cm^3\ g^{-1}$) with a small surface area (96.253 $m^2\ g^{-1}$). According to the IUPAC classification, the adsorption isotherm is an IV-type isotherm, and H3 hysteresis loop which is characteristic of mesoporous materials with cylindrical pores.[2,24,41] The BJH pore size distribution (Fig. 4b) revealed that both materials have mesoporous properties. Also, the figure pointed out that Na/TNTs have a narrow pore size distribution compared to Mag/TNTs with a uniform pore structure ranging from 2.5 nm to 25 nm for Na/TNTs and 3.47 nm to 25 nm for Mag/TNTs, respectively.

3.2. Investigation of the MB adsorption

3.2.1. Effect of pH on the adsorption of MB by Na/TNTs and Mag/TNTs. As illustrated in Fig. 5a, below pH 5, the adsorption capacity of Na/TNTs and Mag/TNTs was 80.5 mg g^{-1} and 88.9 mg g^{-1}, respectively. At pH 5, both Na/TNTs and Mag/TNTs showed the highest adsorption capacity, which reached 134 mg g^{-1} and 99 mg g^{-1}, respectively. Above pH 5, the adsorption capacity decreased gradually. Zeta potential analysis (Fig. 5b) reveals that both materials possess negatively charged surfaces, facilitating MB removal through electrostatic attraction. At pH 5, zeta potential values were −48 mV and −42.8 mV for Na/TNTs and Mag/TNTs, respectively, corresponding to maximum adsorption. Below pH 5, Mag/TNTs showed more negative values (−35.9 mV) than Na/TNTs (−31.4 mV), explaining the higher initial adsorption of Mag/TNTs at low pH. Above pH 5, the negative charge decreased for both materials, consistent with reduced adsorption capacity.

3.2.2. Effect of adsorbent dose on MB removal. The variation of adsorption percentage as a function of adsorbent dosage

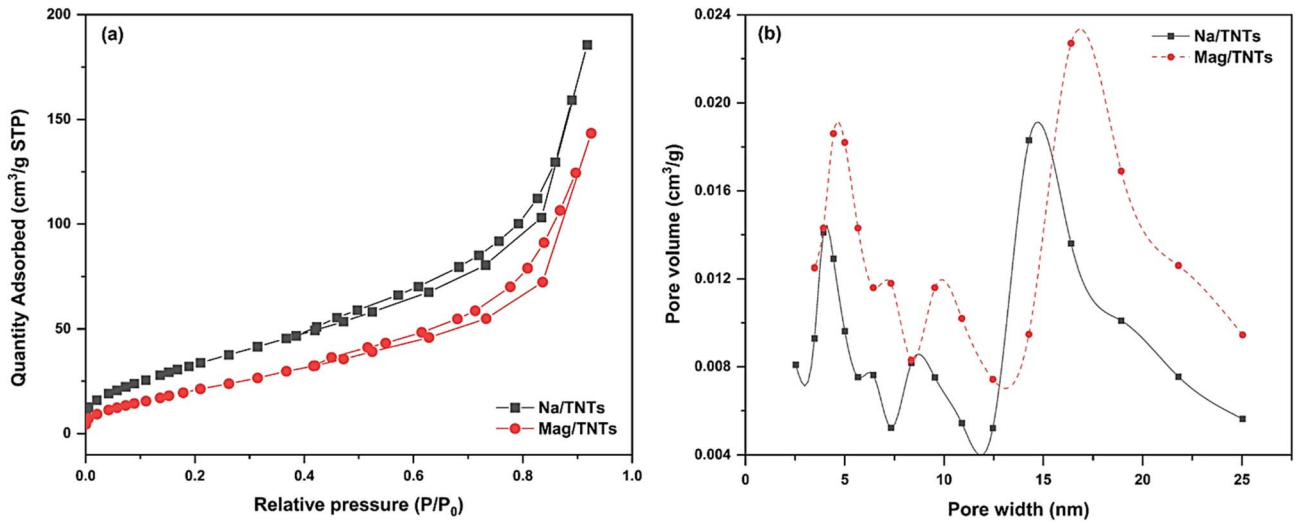

Fig. 4 The nitrogen adsorption/desorption isotherms of Na/TNTs and Mag/TNTs were measured at 77 K; the isotherms are plotted as quantity of adsorbed nitrogen *versus* relative pressure (P/P_0) (a), and BJH pore size distribution curves of Na/TNTs and Mag/TNTs (b).

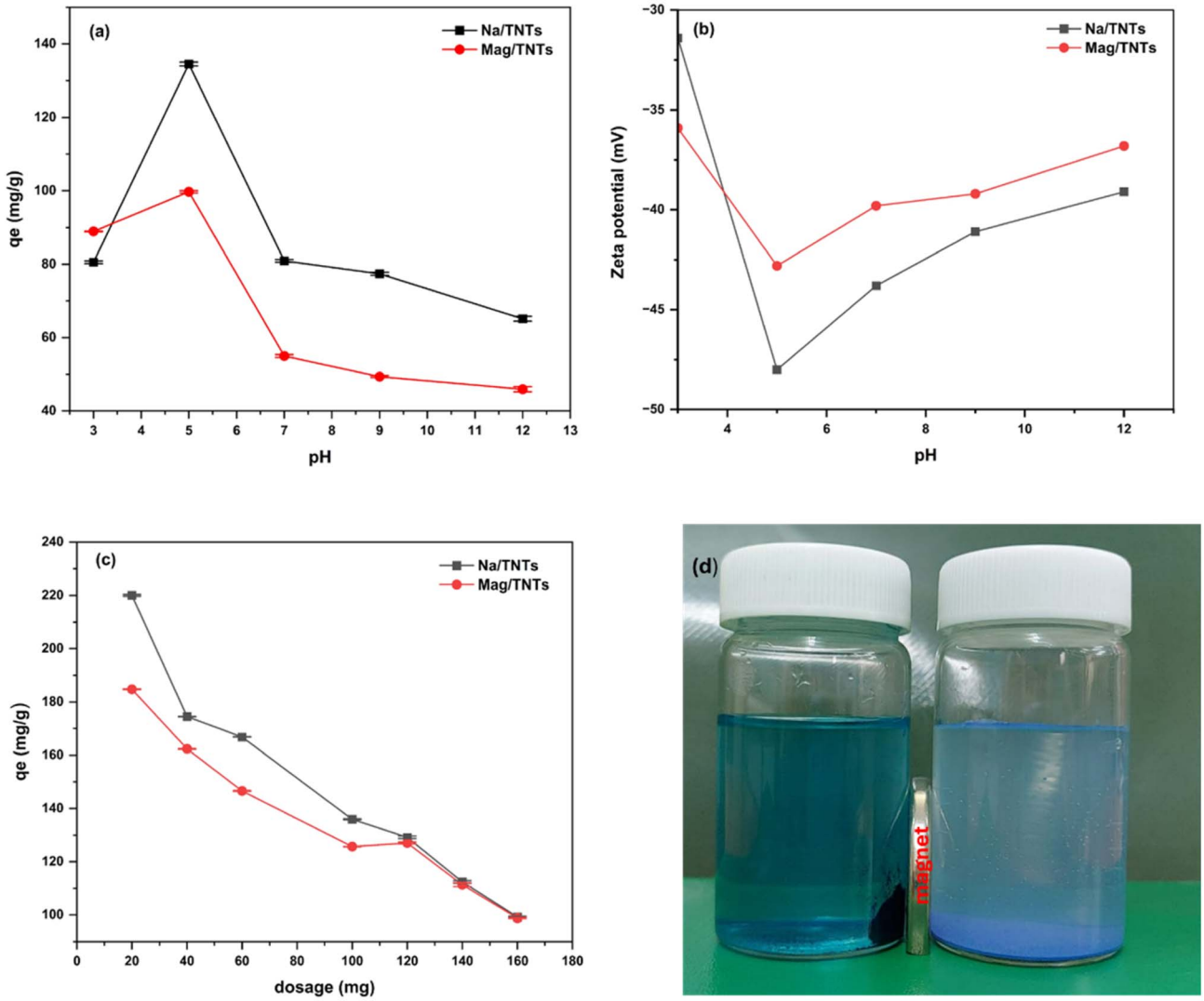

Fig. 5 Effect of pH on the adsorption of MB (a), zeta potential analysis (b), effect of adsorbent dose on the adsorption of MB (c), and a photograph illustrating the influence of an external magnet on the separation of Na/TNTs and Mag/TNTs after MB adsorption (d).

was investigated, as shown in Fig. 5c. The adsorption capacity decreases from 220 mg g^{-1} to 99.2 mg g^{-1} for Na/TNTs and from 184 mg g^{-1} to 98.8 mg g^{-1} for Mag/TNTs as adsorbent dose increased from 20 mg to 160 mg (Fig. 5c). This behavior is due to inefficient utilization of active sites and reduced mass transfer efficiency. At low adsorbent doses, the amount of adsorbent is small compared to the amount of available dye molecules in the solution, and the active sites become effectively occupied. On the other hand, at high adsorbent doses, the number of adsorbent active sites increases while the number of MB dye molecules remains the same. Consequently, many active sites became unoccupied, leading to low adsorption capacity.[42] The magnetic separation behavior of the samples was visually confirmed (Fig. 5d). Mag/TNTs were attracted toward the magnet, while Na/TNTs showed no attraction, indicating the successful incorporation of magnetic properties into the Mag/TNTs.

3.2.3. Effect of contact time. As shown in (Fig. 6), the adsorption capacities of Na/TNTs and Mag/TNTs increased rapidly within the first 30 min, reaching 126.8 mg g^{-1} and 124.4 mg g^{-1}, respectively. A plateau was then observed after approximately 100–150 min. Initially, the active sites on both Na/TNTs and Mag/TNTs were vacant, allowing for rapid adsorption of MB dye. As time progressed, the adsorption rate gradually decreased as these sites became occupied. Eventually, the adsorption process reached equilibrium.[43,44] During the first 10 min, Mag/TNTs exhibited a faster initial adsorption rate than Na/TNTs. However, as the adsorption proceeded, Na/TNTs ultimately achieved a higher adsorption capacity than Mag/TNTs before reaching equilibrium. This behavior may be attributed to the new active sites arising from $CoFe_2O_4$,[45] which promotes faster initial adsorption kinetics. Nevertheless, Na/TNTs achieve a higher equilibrium adsorption capacity due to their larger surface area.

3.2.4. Adsorption kinetics. Adsorption kinetic models were employed to investigate the mass-transfer mechanisms governing the adsorption process and to assess the performance of the adsorbent.[46] Furthermore, the adsorption kinetics can be

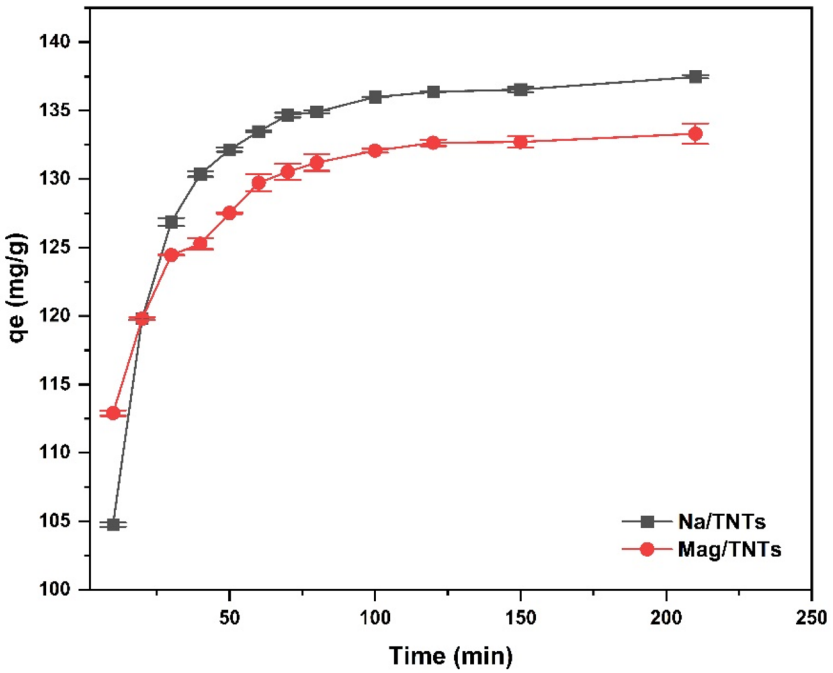

Fig. 6 Effect of time on the adsorption of MB onto Na/TNTs and Mag/TNTs.

interpreted using classical models, including the pseudo-first-order (PFO), pseudo-second-order (PSO), and mixed 1,2-order (MO) models, as well as the Avrami and intraparticle diffusion models.[47,48] The kinetic rate constant, k_2, of the PSO model considers the interaction between the adsorbate molecules and the available adsorption sites, whereas k_1 in PFO represents the rate at which adsorption occurs.[28,46] The MO model integrates the characteristics of PFO kinetics (dependence on unoccupied sites) and PSO kinetics (interaction between adsorbed and free molecules). It assumes that adsorption can occur at any stage of the process, with diffusion or adsorption serving as the rate-controlling step, and considers the initial adsorbate concentration in solution to be randomly distributed.[28,49] The Avrami model focuses on the overall variations in the proportion of occupied adsorption sites throughout time. This depends on the nucleation and growth principle, which suggests that adsorption happens through random nucleation and growth of adsorbates on the surface.[33] Table 1 shows experimental fitting of adsorption data to the adsorption kinetic models, while their equations are presented in Table 2.

Table 1 Kinetic parameters for MB adsorption onto Na/TNTs and Mag/TNTs

Kinetic models	Adjustable parameters	Values		R^2	
		Na/TNTs	Mag/TNTs	Na/TNTs	Mag/TNTs
PFO	k_1	0.139	0.192	0.992	0.990
	q_e	133.9	129.5		
PSO	k_2	0.002	0.0036	0.999	0.998
	q_e	140.5	133.99		
MO	$k_{1,2}$	0.0017	0.0018	0.999	0.998
	q_e	140.1	133.7		
	f_2	0.99	0.99		
Avrami	k_{av}	0.38	0.45	0.992	0.990
	n_{av}	1.35	0.42		
	q_e	133.9	129.5		

Adsorption capacities of 126.8 mg g^{-1} and 124.4 mg g^{-1} were obtained for Na/TNTs and Mag/TNTs, respectively, within the first 30 min, then increased till reaching equilibrium at 100–210 min. The final adsorption capacity (q_t) reached 137.4 mg g^{-1} and 133.3 mg g^{-1} for Na/TNTs and Mag/TNTs at 210 min, respectively. The PSO and MO models provided the best fits to the experimental data, both models yielding correlation coefficients (R^2) of 0.999 for Na/TNTs and 0.998 for Mag/TNTs (Table 1). The excellent fitting of these two models to the experimental data (Fig. 7) suggests that the adsorption proceeds through mixed mechanisms involving both physisorption and chemisorption.[50]

3.2.5. Effect of initial MB concentration and temperature. Fig. 8 shows q_e values of Na/TNTs (a) and Mag/TNTs (b) at different initial concentrations and temperatures. The q_e values increased markedly at low concentrations due to the availability of active adsorption sites on the adsorbent's surface and a high affinity for MB molecules. Afterwards, equilibrium was reached, reflecting the continuous occupation of active adsorption sites and the formation of a monolayer of MB molecules. It is noticeable that the adsorption capacity values increase as the temperature increases. This may be due to the increase in the kinetic energy and mobility of MB molecules at higher temperatures, which subsequently enhances their diffusion through the adsorbents' pores.[28,42,51] Moreover, higher temperatures help prevent the aggregation of dye molecules,[52] which leads to more efficient dye removal.

Table 2 Adsorption isotherm and kinetics models[a]

Isotherm model	Equation	Kinetics model	Equation
Langmuir	$q_e = \frac{q_{max} K_L C_e}{1 + K_L C_e}$	Pseudo-first order	$q_t = q_e(1 - e^{-k_1 t})$
Freundlich	$q_e = K_f C_e^{1/n_f}$	Pseudo-second order	$q_t = \frac{q_e^2 k_2 t}{1 + q_e k_2 t}$
Sips	$q_e = \frac{q_{max} K_S C_e^{1/n_s}}{1 + K_S C_e^{1/n_s}}$	Mixed 1,2-order	$q_t = q_e \frac{1 - e^{-k_{1,2} t}}{1 - f_2 e^{-k_{1,2} t}}$
Langmuir–Freundlich	$q_e = \frac{q_{max}(K_{LF} C_e)^{n_{LF}}}{1 + (K_{LF} C_e)^{n_{LF}}}$	Avrami	$q_t = q_e(1 - e^{(-k_{av} t)^{n_{av}}})$
Dubinin–Radushkevich	$q_e = (q_m)\exp(-K_{ad}\varepsilon^2)$		

[a] q_e: equilibrium adsorption capacity of adsorbent (mg g^{-1}). C_e: equilibrium concentration of the adsorbate (mg L^{-1}). q_{max}: maximum adsorption capacity of adsorbent (mg g^{-1}). K_L: Langmuir constant(L mg^{-1}). K_f: Freundlich constant (L g^{-1}). $1/n_f$: Freundlich adsorption intensity. K_{LF}: equilibrium constant for heterogeneous solid. n_{LF}: heterogeneous parameter. K_S: Sips isotherm model constant (L mg^{-1}). $1/n_s$: Sips isotherm exponent. K_{ad}: Dubinin–Radushkevich constant related to the mean free energy of adsorption (mol^2 J^{-2}). ε: Polyani potential that is related to equilibrium concentration (J mol^{-1}). q_m: Dubinin–Radushkevich monolayer saturation capacity. q_t: adsorption capacity of adsorbent at time t (mg g^{-1}). k_1: rate constant of pseudo first-order model (min^{-1}). k_2: rate constant of pseudo second-order model (g mg^{-1} min^{-1}). $k_{1,2}$: rate constant of mixed 1,2-order model (min^{-1}). t: time (min). k_{av}: Avrami rate constant (min^{-1}). n_{av}: Avrami component (dimensionless).

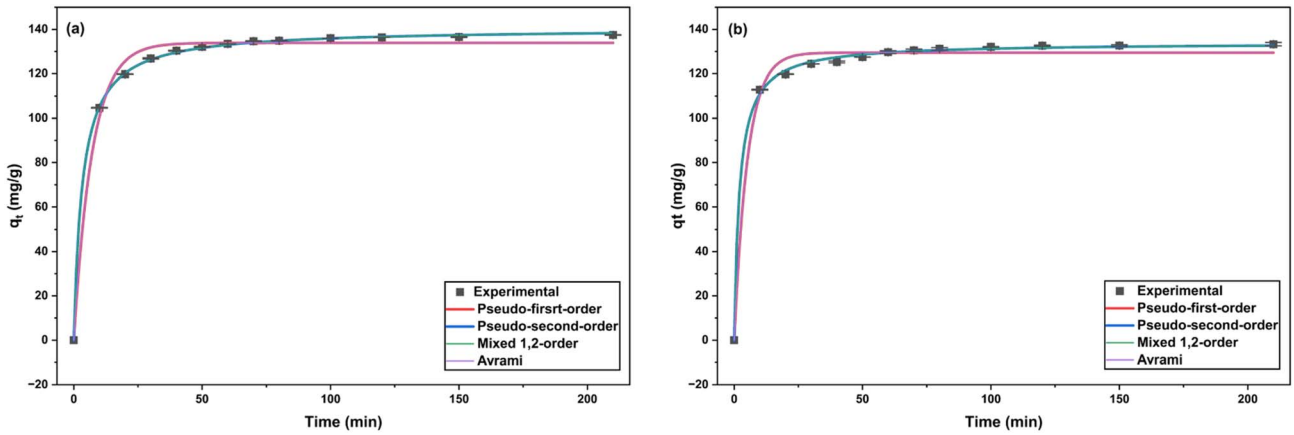

Fig. 7 Fitting experimental data with kinetic models for MB adsorption onto Na/TNTs (a) and Mag/TNTs (b).

3.2.6. Adsorption isotherm. The adsorption isotherm is crucial for explaining the nature of adsorption and its mechanism.[2] It describes the relationship between the adsorption capacity and the solute's equilibrium concentration at a constant temperature.[53] Adsorption isotherm models were employed to correlate the adsorption data. Most models are

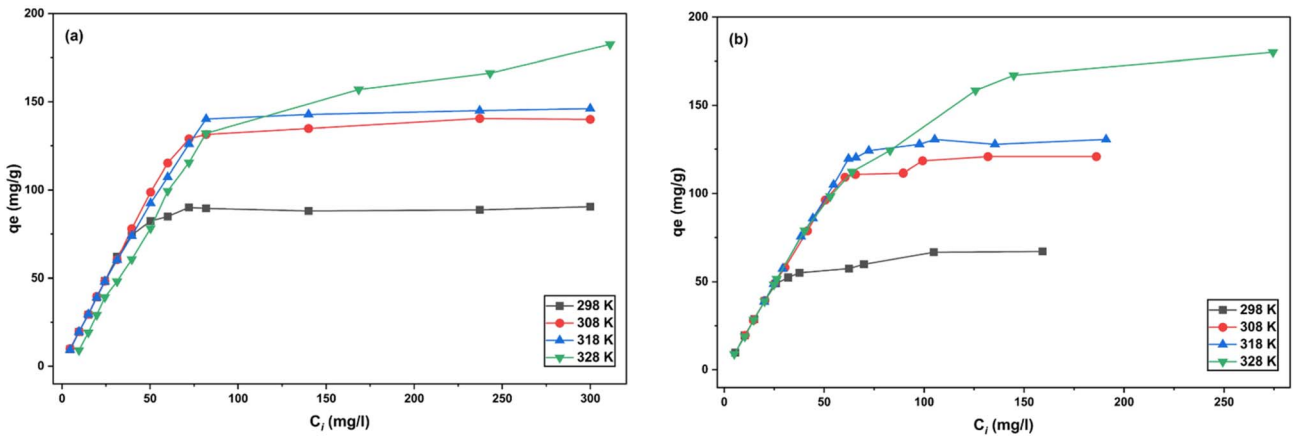

Fig. 8 Effect of initial concentration on the adsorption of MB dye onto Na/TNTs (a) and Mag/TNTs (b) at different temperatures.

based on certain assumptions.[54] The Langmuir isotherm assumes that adsorption takes place on a surface composed of identical, energetically uniform sites, each capable of holding only one adsorbate molecule, with no interactions occurring between the adsorbed species.[55–57] It also determines the maximum adsorption capacity.[58] The Freundlich isotherm

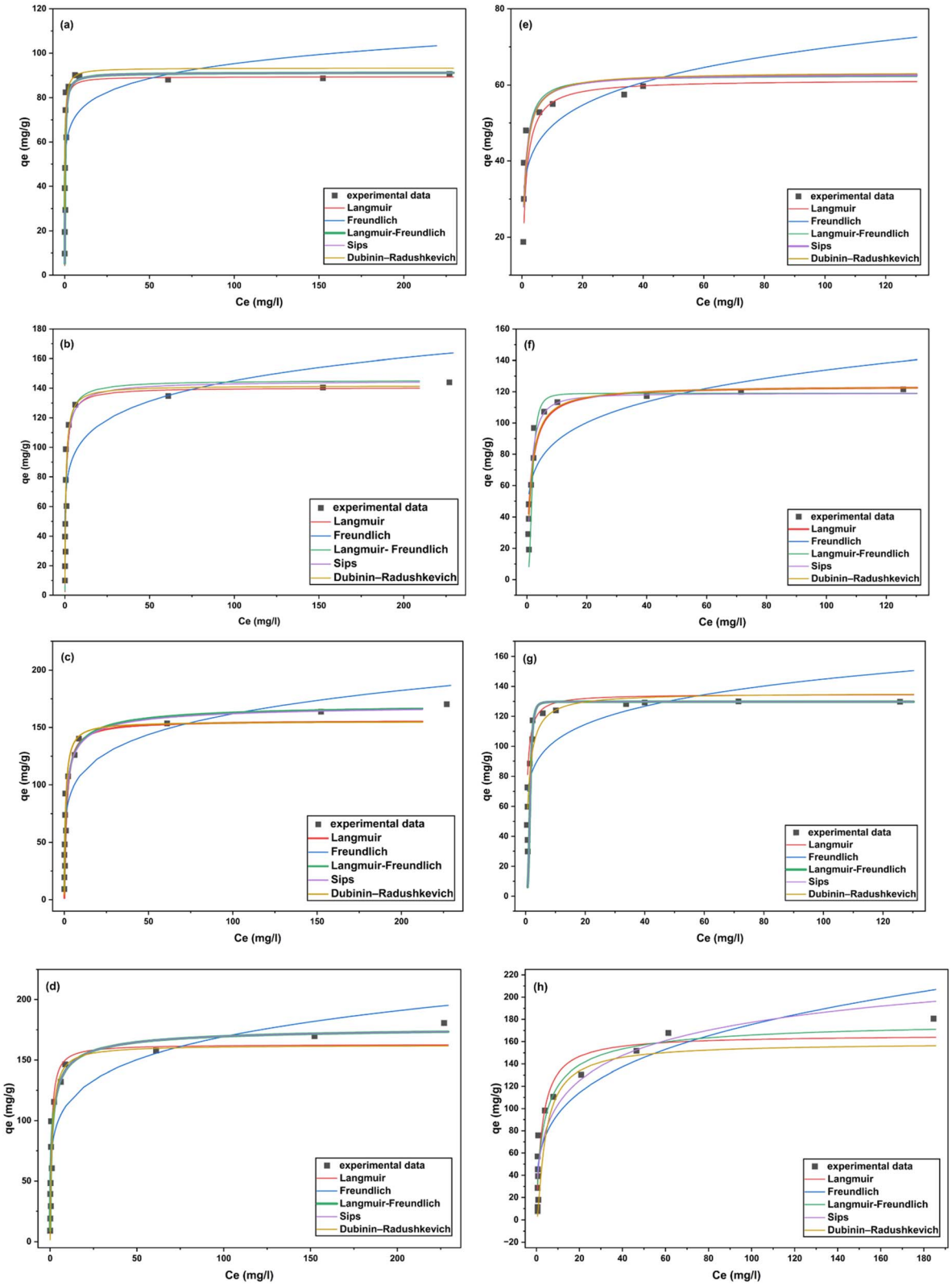

Fig. 9 Fitting experimental q_e data with isothermal models for MB adsorption onto Na/TNTs (a, b, c, d) and Mag/TNTs (e, f, g, h) at different temperatures (298, 308, 318, 328) K.

Table 3 Adsorption isotherm models and their parameters for MB removal using Na/TNTs and Mag/TNTs at different temperatures

		Na/TNTs				Mag/TNTs			
Isotherm model	Parameters	298 K	308 K	318 K	328 K	298 K	308 K	318 K	328 K
Langmuir	q_{max}	89.48	140.52	156.03	163.01	61.4	123.83	134.9	166.2
	K_L	3.97	1.36	0.77	1.32	0.92	0.75	2.2	0.37
	R^2	0.84	0.905	0.93	0.91	0.71	0.93	0.88	0.90
Freundlich	$1/n_f$	0.103	0.145	0.170	0.171	0.15	0.17	0.14	0.26
	K_f	59.15	74.39	73.76	76.75	34.82	58.57	74.1	51.36
	R^2	0.60	0.73	0.84	0.83	0.70	0.73	0.64	0.85
Langmuir–Freundlich	q_{max}	91.23	145.63	172.27	178.98	62.51	119.05	129.78	180.50
	K_{LF}	4.16	1.39	0.83	0.871	1.21	0.55	0.66	0.24
	n_{LF}	0.95	0.93	0.65	0.64	1.084	2.69	3.85	0.75
	R^2	0.83	0.905	0.94	0.93	0.81	0.95	0.91	0.89
Sips	q_{max}	91.23	145.63	172.27	178.98	62.99	119.05	129.78	196.75
	K_S	3.88	1.53	0.91	0.914	1.17	0.77	0.21	0.19
	$1/n_s$	0.95	0.77	0.619	0.648	1.01	1.36	3.85	0.44
	R^2	0.83	0.902	0.94	0.93	0.81	0.95	0.91	0.89
Dubinin–Radushkevich	q_{max}	93.32	141.82	155.26	162.38	63.33	123.73	135.69	159.34
	k_{ad}	5.22×10^{-5}	1.32×10^{-4}	1.59×10^{-4}	2.12×10^{-4}	1.81×10^{-4}	2.48×10^{-4}	1.88×10^{-4}	7.18×10^{-4}
	R^2	0.83	0.904	0.92	0.92	0.81	0.94	0.87	0.90

model describes adsorption as a phenomenon that occurs on a heterogeneous surface through a multilayer adsorption mechanism.[59] The Langmuir–Freundlich (L–F) model is a hybrid isotherm that integrates the heterogeneity assumption of the Freundlich model with the finite-site saturation characteristic of the Langmuir model.[60] The Sips model shares the same mathematical form (Table 2).[61] However, the two models differ in the expression of the heterogeneity parameter. The heterogeneity parameter is written as n_{LF} in the L–F model and as $1/n_s$ in the Sips model.[62] The Sips model predicts a finite monolayer adsorption capacity and addresses the limitations of the Freundlich model at high concentrations.[63] The Dubinin–Radushkevich (D–R) isotherm model is a semi-empirical equation based on the Polanyi potential theory, specifically developed to characterize micropore filling in heterogeneous adsorbents. The equations of the investigated models are reported in Table 2.

Fig. 9 presents the fitting of the experimental adsorption data of MB onto Na/TNTs (a–d) and Mag/TNTs (e–h) at temperatures of 298, 308, 318, and 328 K, respectively, using different isotherm models. The q_e values increase sharply at low C_e values and then reach a plateau. Even though the Langmuir model explains the behavior of monolayer adsorption, the L–F and Sips models fit the data better, indicating adsorption on energetically heterogeneous active sites. The heterogeneous adsorption surface may be due to the presence of magnetic nanoparticles and a nanotubular structure. Conversely, the Freundlich model exhibited a low R^2 (0.60), indicating poor agreement with experimental data and suggesting that a purely empirical multilayer model cannot well explain the adsorption process. The D–R model supports that adsorption includes diffusion into micropore filling in addition to surface coverage. In general, the agreement of these models suggests that MB adsorption onto both Na/TNTs and Mag/TNTs occurs *via* a mechanism that includes pore filling, heterogeneous multi-energy interactions, and monolayer adsorption on active sites. In addition, the Langmuir–Freundlich and Sips models show consistently strong agreement with the experimental data at all other investigated temperatures, as supported by the R^2 values presented in Table 3 for both Na/TNTs and Mag/TNTs. The strong alignment of experimental data with the fitted models demonstrates the reliability and validity of the isothermal analysis. The q_{max} values Na/TNTs increased from (91.23 to 178.98) mg g^{-1} as the temperature increased from (298to 328) K, whereas Mag/TNTs showed a similar but more pronounced enhancement from (62.51 to 180.50) mg g^{-1}, as obtained from the L–F model. The sharper increase observed for Mag/TNTs indicates that the incorporation of magnetic components enhances the thermal activation of adsorption sites and strengthens the adsorbate–adsorbent interactions at elevated temperatures.[64,65]

3.3. Adsorption thermodynamics

A thermodynamic analysis was conducted to further evaluate the feasibility of MB adsorption onto Na/TNTs and Mag/TNTs, as well as the associated energetic changes. Several thermodynamic parameters were determined to provide a better understanding of the adsorption mechanism, including the thermodynamic equilibrium constant (K_{eq}) and the standard Gibbs free energy of adsorption (ΔG°) at each temperature, along with the standard enthalpy (ΔH°) and entropy (ΔS°) of adsorption. These parameters were estimated using eqn (4)–(7).[52,66]

$$K_{eq} = \frac{1000 \times K_{LF} \times M \times \text{dye standard conc}}{\gamma} \quad (4)$$

$$\Delta G^\circ = -RT \ln K_{eq} \quad (5)$$

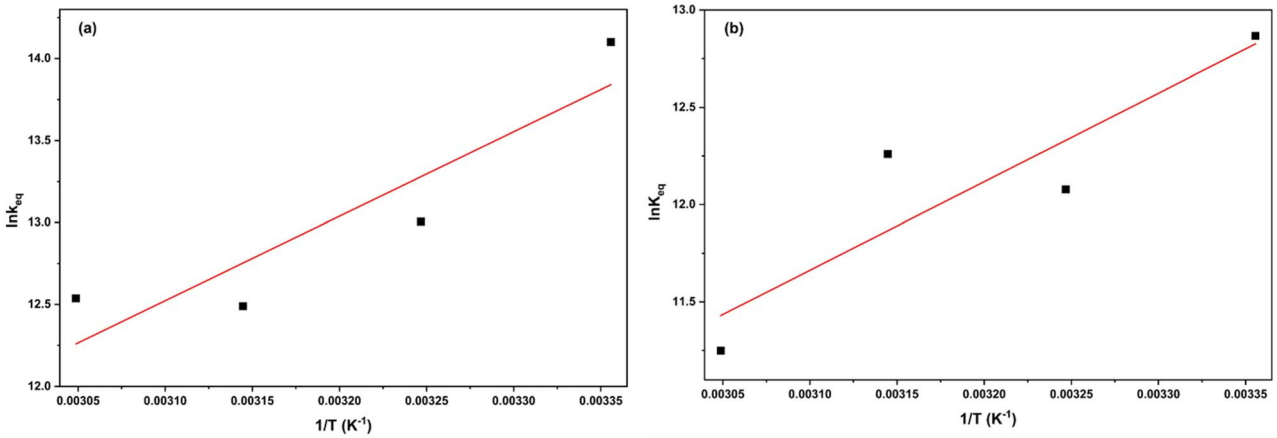

Fig. 10 The Van't Hoff plot for MB adsorption onto Na/TNTs (a) and Mag/TNTs (b).

$$\Delta G^{\circ} = \Delta H^{\circ} - T\Delta S^{\circ} \quad (6)$$

$$\ln K_{eq} = \frac{\Delta S^{\circ}}{R} - \frac{\Delta H^{\circ}}{RT} \quad (7)$$

where γ, M (g mol^{-1}), and R represent the activity coefficient, the molar mass, and the universal gas constant with values 1.00, 319.859 g mol^{-1}, and 8.314 J mol^{-1} K^{-1}, respectively. The standard concentration of the dye adsorbate was taken as 1 mol L^{-1}, and T represents the absolute temperature in Kelvin. The thermodynamic parameters of the adsorption process were determined from the Van't Hoff plots of $\ln K_{eq}$ *versus* $1/T$ for both Na/TNTs and Mag/TNTs (Fig. 10). The linear regression yielded R^2 values of 0.82 for Na/TNTs and 0.81 for Mag/TNTs, indicating that the adsorption process does not fully conform to ideal Van't Hoff behavior. Such deviations typically arise from heterogeneous adsorption sites or temperature-dependent adsorption pathways.[67] Consequently, the derived thermodynamic parameters should be interpreted with caution, and the uncertainties (standard errors) are provided to reflect the limited precision of the linear fit. Table 4 reports the thermodynamic parameters along with their associated standard errors. The uncertainties in ΔG° were propagated from the errors in ΔH° and ΔS°. From the slope and intercept of the line, the ΔH° and ΔS° were calculated, respectively. The relatively large standard errors for ΔH° and ΔS° reflect the limited precision of the linear fit.

The nature of the adsorption process, whether exothermic or endothermic, is determined by the positive or negative value of ΔH°. The sign and magnitude of ΔS° indicate the degree of randomness at the solid–solution interface.[68] Moreover, the ΔG° provides insights into the spontaneity of the adsorption process at various temperatures.[69] The ΔG° values for both adsorbents were negative at all studied temperatures (Table 4), indicating that the adsorption process is spontaneous. The negative ΔH° values confirm that the adsorption process is exothermic for both materials. Additionally, the negative ΔS° values suggest a decrease in randomness at the solid–solution interface during adsorption. Although the negative ΔH° and ΔS° values indicate an exothermic process with reduced interfacial randomness, the adsorption capacity increased with temperature. This suggests that although the process is thermodynamically exothermic, the overall adsorption performance is governed primarily by kinetic and diffusion effects,[28,42,51,70] which is consistent with the trends observed in our concentration and temperature studies.

3.4. Adsorbent reusability

The adsorption capacity of Na/TNTs and Mag/TNTs showed a slight decrease after five successive regeneration cycles during the removal of MB, as explained in Fig. 11, with values of (78.7 and 78.6, 71.5 and 69.5, 71.06) mg g^{-1} and (68.2, 70.7, and 67.3, and 65.2 and 61.8) mg g^{-1}, respectively. The results confirmed their good reusability and potential as efficient adsorbents for wastewater treatment applications.

This study presents a comparative analysis of sodium titanate nanotubes with other related materials of the same chemical structure for the removal of MB dye. In our research,

Table 4 Values of the thermodynamic parameters for the adsorption of MB onto Na/TNTs and Mag/TNTs

	Na/TNTs				Mag/TNTs			
T (K)	ΔG° (kJ mol^{-1})	ΔH° (kJ mol^{-1})	ΔS° (J mol^{-1} K^{-1})	R^2	ΔG° (kJ mol^{-1})	ΔH° (kJ mol^{-1})	ΔS° (J mol^{-1} K^{-1})	R^2
298	−34.3 ± 1.7	−42.9 ± 13.8	−28.8 ± 44.3	0.82	−31.8 ± 1.6	−37.9 ± 12.9	−20.4 ± 41.4	0.81
308	−34.0 ± 1.7	—	—	—	−31.6 ± 1.6	—	—	—
318	−33.7 ± 1.7	—	—	—	−31.4 ± 1.6	—	—	—
328	−33.4 ± 1.7	—	—	—	−31.2 ± 1.6	—	—	—

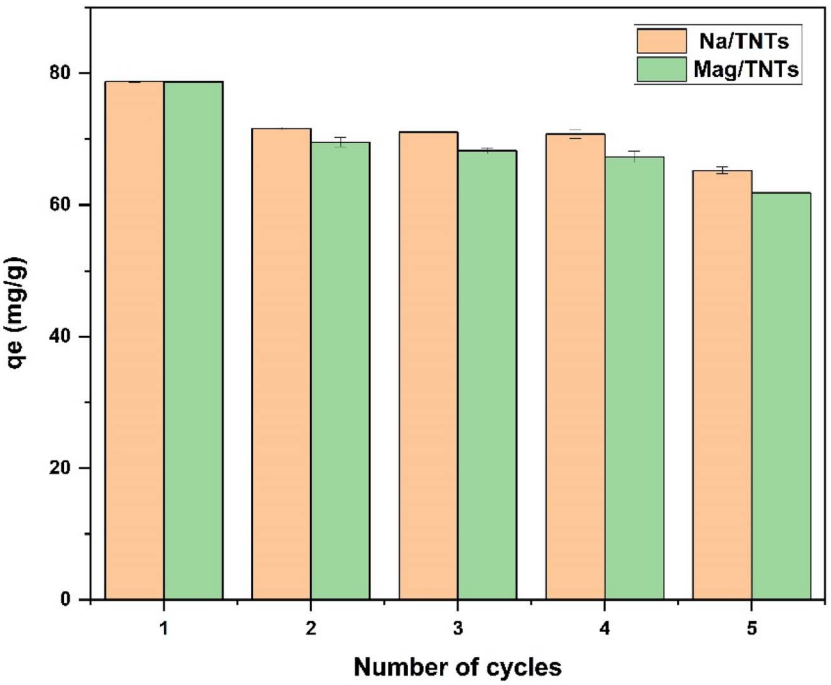

Fig. 11 Regeneration of Na/TNTs and Mag/TNTs adsorbents for MB removal.

Table 5 The reported equilibrium adsorption capacities of titanate nanotubes as an adsorbent for MB

Adsorbent	Adsorption capacity (mg g^{-1})	Reference
Graphene oxide/$ZnTiO_3$/TiO_2	78	71
Activated carbon fiber supported titanate nanotubes (ACF@TNTs)	32.7	72
H-TNT and H-TNS ($H_2Ti_3O_7$)	7.25 and 6.67	73
Na–$BaLa_4Ti_4O_{15}$	37.6	74
Cerium titanate cellulose fiber nanocomposite (Ce–Ti/Cf)	54.29	75
Titanate nanotube (TNTs)	151.51	76
Potassium titanate (K_2TiO_3)	21.92	77
Carbonaceous mesoporous titanate-based materials ($Na_2Ti_3O_7$/$Na_3Ti_6O_{13}$)	27.5	78
Activated charcoal-supported TNTs (TNTs@PAC)	173.30	79
Na/TNTs	178.98 (at 328 K)	Our study
Mag/TNTs	180.5 (at 328 K)	Our study

TNTs showed higher adsorption capacity than other adsorbents listed in Table 5, and for the first time, Mag/TNTs were used for dye removal, showing significant adsorption efficiency.

3.5. Mechanism of MB adsorption

MC simulations were employed to estimate the adsorption sites and energies of a single MB molecule, a monolayer, and multilayers of MB dye on the $Na_2Ti_3O_7$ and $CoFe_2O_4$ surfaces. The corresponding adsorption energies were -109.37 kcal mol^{-1} for $Na_2Ti_3O_7$ and -446.33 kcal mol^{-1} for $CoFe_2O_4$, respectively. These values are significantly higher than typical experimental adsorption enthalpies for dye removal, which is explained by several factors. First, the calculated energy represents the sum of multiple simultaneous interactions per MB molecule. As shown in Fig. 12, when a single MB molecule attaches to the surface, its hydrogen atoms (from methyl or aromatic groups) form favorable electrostatic interactions with surface oxygen atoms. These interactions occur at distances of 2.58–2.97 Å for $Na_2Ti_3O_7$ and 2.3–2.8 Å for $CoFe_2O_4$. Additionally, metal–π interactions were observed, wherein the aromatic rings of MB orient parallel to surface metal atoms. Specifically, interactions were identified between the Ti atoms in $Na_2Ti_3O_7$ (Fig. 12A) and the Fe atoms in $CoFe_2O_4$ (Fig. 12B) with the aromatic ring of the dye. The distances between the centroid of the benzenoid moiety of MB and the Ti and Fe were approximately 4.3 Å and 3.5 Å, respectively. These interaction distances are consistent with those reported for similar systems in the Cation–Aromatic Database (CAD), where cation–π distances typically range from 3.5 to 4.5 Å.[80] Second, the simulation uses clean surfaces with a high density of unsaturated-coordinated metal and oxygen atoms, which are more reactive than fully coordinated surface sites found under experimental conditions. Consequently, each dye molecule simultaneously forms multiple contacts with the surface, and

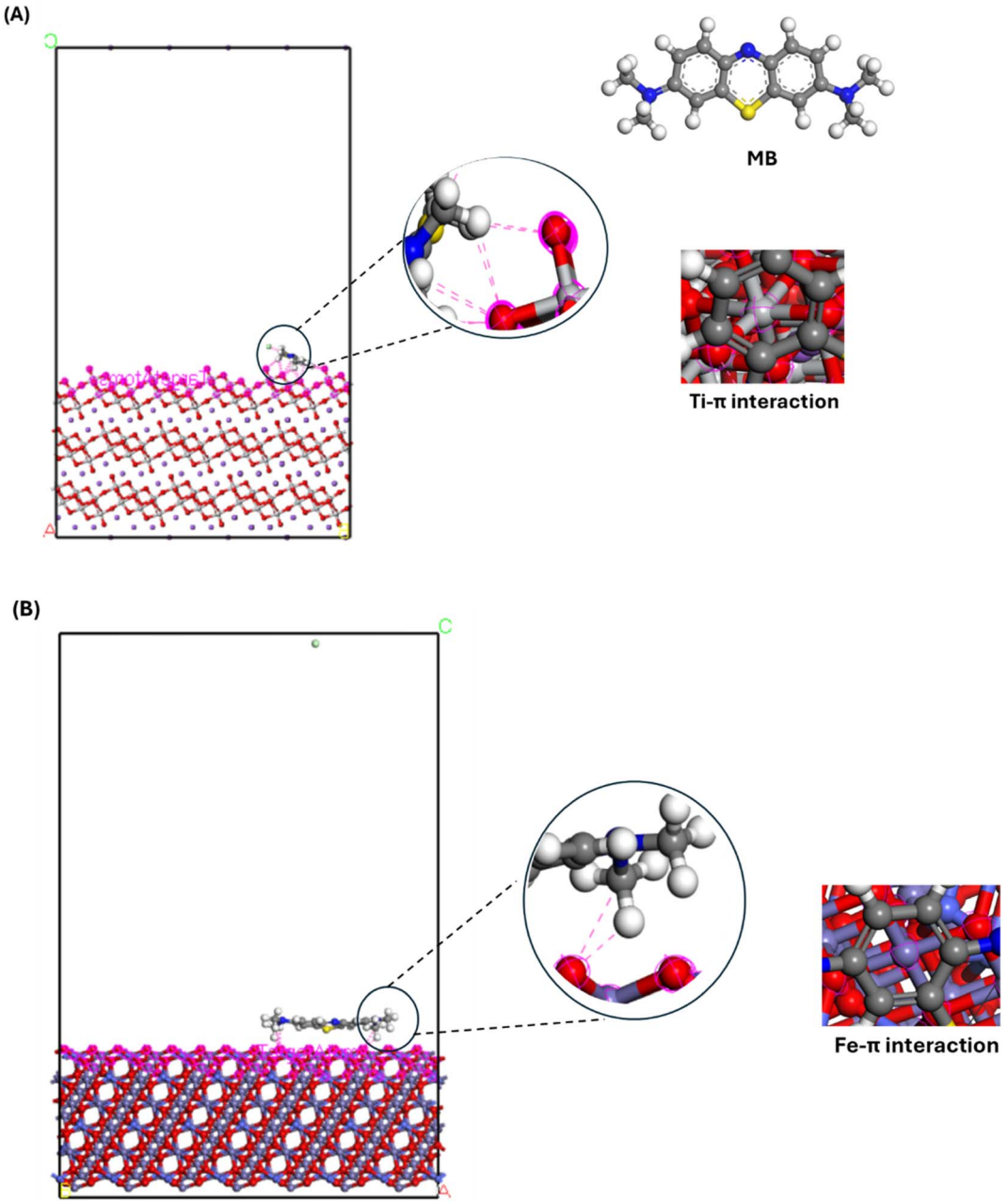

Fig. 12 The lowest-energy structure of the adsorption of a single MB dye molecule on the surface of $Na_2Ti_3O_7$ (A) and $CoFe_2O_4$ (B).

the calculated adsorption energy represents the cumulative sum of all these individual interactions. Third, the calculations are performed in vacuum, completely omitting the dielectric screening effect of water molecules and the competition from solvent molecules for adsorption sites. In aqueous solution, competition from water molecules and charge screening will significantly reduce the net adsorption energy. Consequently, these values should not be directly compared to experimental free energies of adsorption; instead, they are useful for comparing relative binding affinities and identifying interaction geometries. Although $Na_2Ti_3O_7$ exhibits weaker interactions with MB, as indicated by its lower adsorption energies compared to $CoFe_2O_4$, its experimentally confirmed higher surface area facilitates the adsorption of a greater number of MB molecules. This accounts for the higher removal efficiency of $Na_2Ti_3O_7$ observed experimentally.

Fig. 13 illustrates the lowest-energy configuration of a monolayer composed of 14 MB dye molecules adsorbed on the surfaces of $Na_2Ti_3O_7$ and $CoFe_2O_4$. This configuration was selected to elucidate both dye–surface and dye–dye interactions. In the side view, close contacts are observed between the methyl or aromatic hydrogen atoms of MB with the surface oxygen atoms, with interaction distances ranging from 2.48 Å to 2.95 Å for $Na_2Ti_3O_7$, and from 2.29 Å to 2.81 Å for $CoFe_2O_4$. Furthermore, metal–π interactions are evident, where the aromatic rings of MB align parallel to surface metal atoms, specifically Ti in $Na_2Ti_3O_7$ and

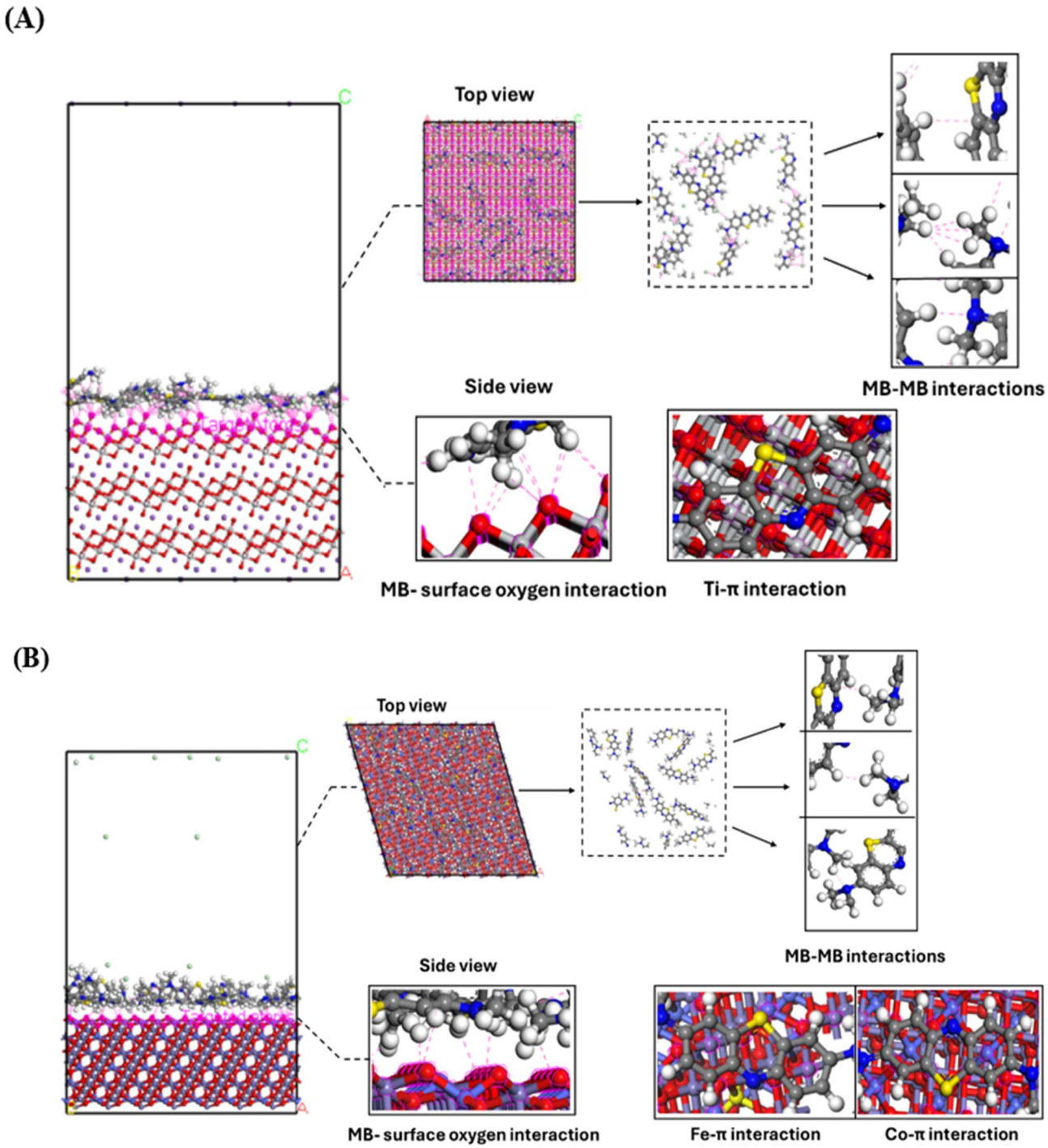

Fig. 13 The lowest-energy structure of the adsorption of 14 MB dye molecules (monolayer) on the surface of $Na_2Ti_3O_7$ (A) and $CoFe_2O_4$ (B).

Fe/Co in $CoFe_2O_4$. In the top view, intermolecular attractions between adjacent dye molecules are apparent. These include van der Waals interactions between methyl hydrogen atoms and either other methyl hydrogens or the aromatic ring hydrogens/carbons of neighboring molecules. The distances associated with these interactions range from 2.46 Å to 2.95 Å for $Na_2Ti_3O_7$ and from 2.34 Å to 2.55 Å for $CoFe_2O_4$.

Fig. 14 presents the lowest-energy configuration of 28 MB dye molecules adsorbed as a multilayer on the surfaces of $Na_2Ti_3O_7$ and $CoFe_2O_4$. This configuration primarily illustrates the intermolecular interactions (MB–MB) within the multilayer structure formed on the adsorbent surfaces. In the side view, interactions are observed between the methyl and aromatic hydrogen atoms of the dye molecules and the surface oxygen atoms, with distances ranging from 2.66 Å to 2.98 Å for $Na_2Ti_3O_7$ and from 2.31 Å to 2.85 Å for $CoFe_2O_4$. The top view reveals multiple modes of MB–MB interaction. These include van der Waals forces between methyl hydrogen atoms and either other

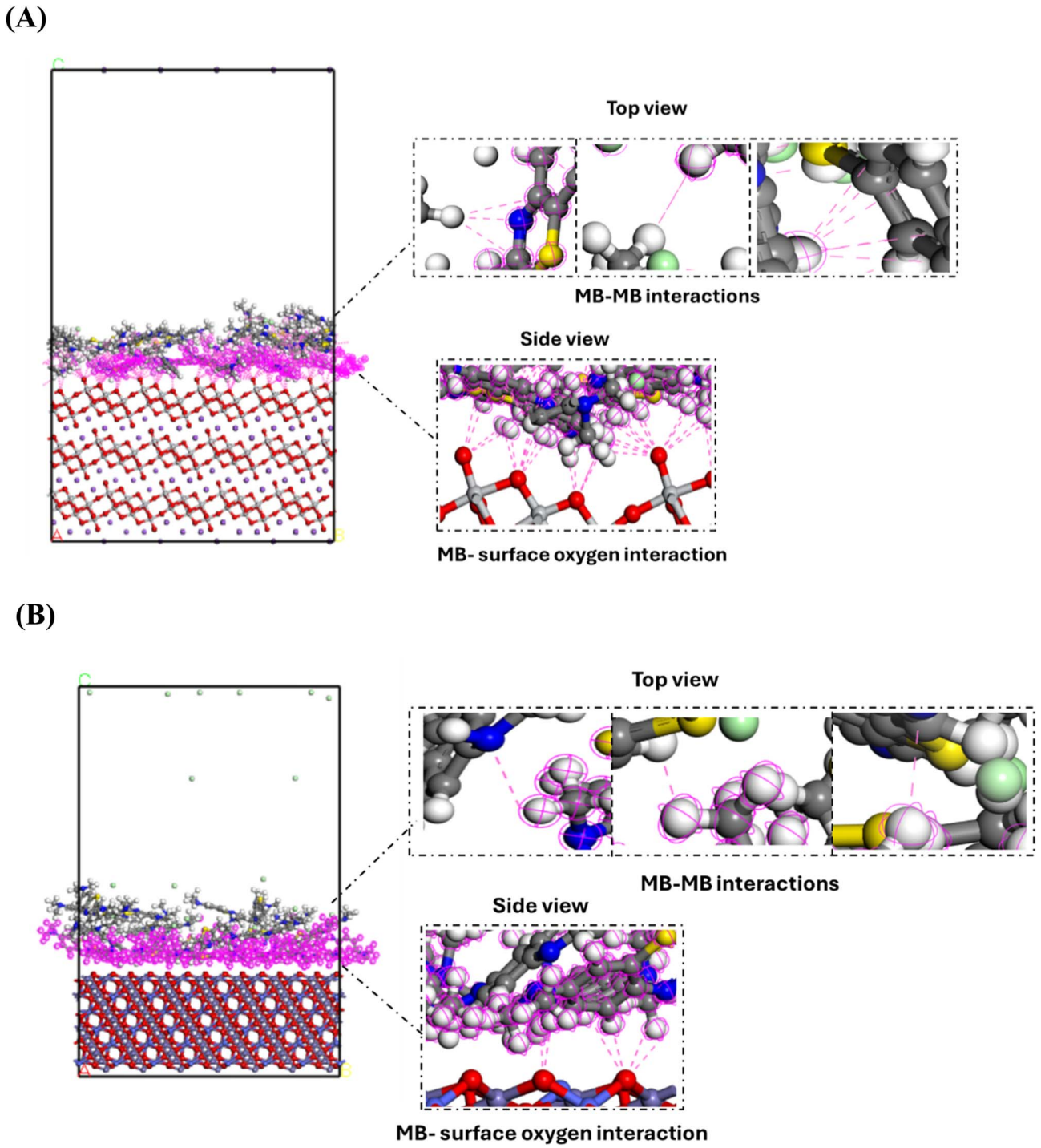

Fig. 14 The lowest-energy structure of the adsorption of 28 MB dye molecules (multilayer) on the surface of $Na_2Ti_3O_7$ (A) and $CoFe_2O_4$ (B).

methyl hydrogens or aromatic ring hydrogens/carbons. The corresponding interaction distances range from 2.20 Å to 2.97 Å for $Na_2Ti_3O_7$ and from 2.07 Å to 2.37 Å for $CoFe_2O_4$.

4. Conclusion

In this study, Na/TNTs and Mag/TNTs were successfully prepared *via* hydrothermal method. The incorporation of cobalt ferrite into titanate nanotubes enhanced the rate of adsorption of MB dye and allowed easy separation. The synthesized nanotubes were characterized by SEM, HR-TEM, FTIR, BET, XRD, and zeta potential analysis. Na/TNTs and Mag/TNTs exhibited effective performance in the adsorption of MB dye, with adsorption capacities of (90.5, 146.1, 171.9, and 182.4) mg g^{-1} for Na/TNTs and (67, 120.8, 130.5, and 180) mg g^{-1} for Mag/TNTs at pH 5 and different temperatures (298, 308, 318, 328) K. Various parameters were studied to optimize the MB dye adsorption, such as pH, adsorbent dose, initial MB concentration, temperature, time, and adsorbent reusability.

Isotherm models were used to fit the adsorption data obtained at different concentrations. In general, the best-fitting models for Na/TNTs and Mag/TNTs were Langmuir–Freundlich, Sips, and Dubinin–Radushkevich at the investigated temperature, indicating that the adsorbent materials possess heterogeneous surfaces and exhibit saturated monolayer adsorption behavior. Additionally, the pseudo-first-order, pseudo-second order, mixed 1,2-order, and Avrami models were employed to fit the experimental kinetic data. Among these models, the pseudo-second order and mixed 1,2-order models provided the best fit to the experimental results, implying that the adsorption proceeds through mixed mechanisms involving both physisorption and chemisorption. MC simulations revealed that although $CoFe_2O_4$ exhibits stronger individual interactions with MB dye, $Na_2Ti_3O_7$ demonstrates higher overall dye removal efficiency, attributed to its larger surface area. The adsorption geometries confirmed favorable electrostatic and metal–π–π interactions, particularly between the hydrogen/aromatic rings of MB and the surface oxygen or metal atoms. In both monolayer and multilayer configurations, MB–MB interactions, primarily van der Waals forces, play a crucial role in stabilizing the adsorbed structures. These findings highlight the combined influence of surface characteristics and intermolecular interactions in governing the adsorption behavior of MB dye. Although Na/TNTs exhibited higher removal efficiency than Mag/TNTs, this work paves the way for the design of efficient magnetic titanate composites for wastewater treatment.

Author contributions

Rania N. Zohny: writing–original draft, visualization, software, investigation, formal analysis, data curation. Ayman H. Zaki: conceptualization, methodology, investigation, supervision, writing review & editing. A. A. Farghali: supervision. Mohamed Taha: writing– review & editing, visualization, supervision, software, methodology, investigation, conceptualization.

Conflicts of interest

The authors declare that they have no known competing financial interests or personal relationships that could have appeared to influence the work reported in this paper.

Data availability

All data generated or analysed during this study are included in the manuscript.

Supplementary information (SI) is available. See DOI: https://doi.org/10.1039/d6ra02268e.

Acknowledgements

All gratitude to the Academy of Scientific Research and Technology (ASRT) in Egypt for their valuable financial support for this work. Scientists of the next generation (SNG) scholarship, Cycle 8.

References

1 J. A. Aznar-Sánchez, L. J. Belmonte-Ureña, J. F. Velasco-Muñoz and F. Manzano-Agugliaro, *J. Cleaner Prod.*, 2018, **198**, 1120–1132.
2 R. Saleh, A. H. Zaki, F. I. A. El-Ela, A. A. Farghali, M. Taha and R. Mahmoud, *J. Environ. Chem. Eng.*, 2021, **9**, 104726.
3 N. Zolkefli, S. S. Sharuddin, M. Z. M. Yusoff, M. A. Hassan, T. Maeda and N. Ramli, *Water*, 2020, **12**, 3417.
4 M. K. Hasan, A. Shahriar and K. U. Jim, *Heliyon*, 2019, **5**, e02145.
5 V. K. Garg, M. Amita, R. Kumar and R. Gupta, *Dyes Pigm.*, 2004, **63**, 243–250.
6 F. D. Chequer, G. R. De Oliveira, E. A. Ferraz, J. C. Cardoso, M. B. Zanoni and D. P. De Oliveira, *Eco-Friendly Text. Dyeing Finish.*, 2013, **6**, 151–176.
7 V. Katheresan, J. Kansedo and S. Y. Lau, *J. Environ. Chem. Eng.*, 2018, **6**, 4676–4697.
8 S. Dardouri and J. Sghaier, *Korean J. Chem. Eng.*, 2017, **34**, 1037–1043.
9 P. O. Oladoye, T. O. Ajiboye, E. O. Omotola and O. J. Oyewola, *Results Eng.*, 2022, 100678.
10 R. Ahmad and R. Kumar, *J. Environ. Manage.*, 2010, **91**, 1032–1038.
11 B. Mu and A. Wang, *J. Environ. Chem. Eng.*, 2016, **4**, 1274–1294.
12 A. S. Abdulhameed, A. H. Jawad and A.-T. Mohammad, *Bioresour. Technol.*, 2019, **293**, 122071.
13 L. Ceroni, S. Benazzato, S. Pressi, L. Calvillo, E. Marotta and E. Menna, *Nanomaterials*, 2024, **14**, 522.
14 M. Aaddouz, K. Azzaoui, N. Akartasse, E. Mejdoubi, B. Hammouti, M. Taleb, R. Sabbahi and S. Alshahateet, *J. Mol. Struct.*, 2023, **1288**, 135807.
15 M. H. Kahsay, *Appl. Water Sci.*, 2021, **11**, 45.
16 A. K. Inamdar, N. R. Hulsure, A. S. Kadam, R. S. Rajenimbalkar, R. Karpoormath, S. B. Shelke and S. N. Inamdar, *Results Chem.*, 2023, **5**, 100854.
17 T. Tatarchuk, N. Paliychuk, R. B. Bitra, A. Shyichuk, M. Naushad, I. Mironyuk and D. Ziółkowska, *Desalin. Water Treat.*, 2019, **150**, 374–385.
18 M. Hinojosa-Reyes, R. Camposeco-Solis and F. Ruiz, *Microporous Mesoporous Mater.*, 2019, **276**, 183–191.
19 X. Lei, X. Li, Z. Ruan, T. Zhang, F. Pan, Q. Li, D. Xia and J. Fu, *J. Mol. Liq.*, 2018, **266**, 122–131.
20 T. Tuutijärvi, J. Lu, M. Sillanpää and G. Chen, *J. Hazard. Mater.*, 2009, **166**, 1415–1420.
21 H. Jing, C. G. Hua and I. Lo, *Water Res.*, 2005, **39**, 4528–4536.
22 S. J. Salih and Z. S. Tahseen, *Next Sustain.*, 2026, **7**, 100240.
23 P. A. Vinosha, A. Manikandan, A. C. Preetha, A. Dinesh, Y. Slimani, M. A. Almessiere, A. Baykal, B. Xavier and G. F. Nirmala, *J. Supercond. Novel Magn.*, 2021, **34**, 995–1018.
24 S. Kumar, F. Ahmed, N. M. Shaalan, R. Kumar, A. Alshoaibi, N. Arshi, S. Dalela, F. Sayeed, S. Dwivedi and K. Kumari, *Materials*, 2022, **15**, 7955.
25 A. Zaki, M. A. Hafiez, W. M. El Rouby, S. El-Dek and A. Farghali, *J. Magn. Magn. Mater.*, 2019, **476**, 207–212.

26 J. Zhu, Q. Liu, Z. Li, J. Liu, H. Zhang, R. Li and J. Wang, *J. Hazard. Mater.*, 2018, **353**, 9–17.
27 Y. Hu, C. Zou, T. Xiong and H. Wang, *J. Ind. Eng. Chem.*, 2023, **128**, 294–305.
28 A. Abdelkarim, A. H. Zaki, S. I. El-Dek and M. Taha, *J. Mol. Liq.*, 2024, **415**, 126414.
29 A. Jain, S. P. Ong, G. Hautier, W. Chen, W. D. Richards, S. Dacek, S. Cholia, D. Gunter, D. Skinner and G. Ceder, *APL Mater.*, 2013, **1**, 011002.
30 H. Sun, Z. Jin, C. Yang, R. L. Akkermans, S. H. Robertson, N. A. Spenley, S. Miller and S. M. Todd, *J. Mol. Model.*, 2016, **22**, 1–10.
31 M. Makowska-Janusik, K. Filipecka-Szymczyk, D. Pelczarski, W. Stampor and M. Zalas, *Molecules*, 2025, **30**, 1312.
32 D. Delahaye, S. Chaimatanan and M. Mongeau, in *Handbook of Metaheuristics*, Springer, 2018, pp. 1–35.
33 E. S. Elbanna, A. A. Farghali, M. H. Khedr and M. Taha, *J. Mol. Liq.*, 2024, **409**, 125538.
34 W. Gao, Y. Chen, B. Li, S.-P. Liu, X. Liu and Q. Jiang, *Nat. Commun.*, 2020, **11**, 1196.
35 B. B. Majumdar, V. Prytkova, E. K. Wong, J. A. Freites, D. J. Tobias and M. Heyden, *J. Chem. Theory Comput.*, 2019, **15**, 1399–1408.
36 B. Verberck, in *Applications of Monte Carlo Method in Science and Engineering*, IntechOpen, 2011.
37 N. M. Refat, M. Y. Nassar and S. A. Sadeek, *RSC Adv.*, 2022, **12**, 25081–25095.
38 A. H. Zaki and M.-J. Lee, *ACS Omega*, 2019, **4**, 19623–19634.
39 M. Morsy, A. I. Abdel-Salam, D. A. Rayan, I. Gomaa and A. Elzwawy, *J. Nanopart. Res.*, 2022, **24**, 226.
40 A. H. Zaki, A. A. Naeim and S. I. El-Dek, *Environ. Sci. Pollut. Res.*, 2019, **26**, 36388–36400.
41 Y. Zhang, D. Shao, J. Yan, X. Jia, Y. Li, P. Yu and T. Zhang, *J. Nat. Gas Geosci.*, 2016, **1**, 213–220.
42 B. S. Yadav and S. Dasgupta, *Inorg. Chem. Commun.*, 2022, **137**, 109203.
43 H. Ighnih, R. Haounati, H. Ouachtak, A. Regti, B. El Ibrahimi, N. Hafid, A. Jada, M. L. Taha and A. A. Addi, *Inorg. Chem. Commun.*, 2023, **153**, 110886.
44 H. Ouachtak, R. El Haouti, A. El Guerdaoui, R. Haounati, E. Amaterz, A. A. Addi, F. Akbal and M. L. Taha, *J. Mol. Liq.*, 2020, **309**, 113142.
45 Z. Iqbal, M. S. Tanweer and M. Alam, *ACS Omega*, 2023, **8**, 6376–6390.
46 J. Wang and X. Guo, *J. Hazard. Mater.*, 2020, **390**, 122156.
47 K. Tan and B. Hameed, *J. Taiwan Inst. Chem. Eng.*, 2017, **74**, 25–48.
48 J. Wang and X. Guo, *Chemosphere*, 2022, **309**, 136732.
49 X. Guo, Y. Liu and J. Wang, *Mar. Pollut. Bull.*, 2019, **145**, 547–554.
50 E. P. Komarala, S. Doshi, S. Thiyagarajan, M. Aslam and D. Bahadur, *New J. Chem.*, 2018, **42**, 129–136.
51 W. Jia, L. Sun, H. Li, T. Lv, Y. Tang and Y. Pi, *Front. Mar. Sci.*, 2025, **12**, 1542584.
52 B. M. Thamer, F. A. Al-Aizari and H. S. Abdo, *Molecules*, 2023, **28**, 7712.
53 R. Gopinathan, A. Bhowal and C. Garlapati, *J. Chem. Thermodyn.*, 2017, **107**, 182–188.
54 G. K. Rajahmundry, C. Garlapati, P. S. Kumar, R. S. Alwi and D.-V. N. Vo, *Chemosphere*, 2021, **276**, 130176.
55 I. Narin, Y. Surme, M. Soylak and M. Dogan, *J. Hazard. Mater.*, 2006, **136**, 579–584.
56 S. N. Shankar, D. R. Dinakaran, D. K. Chandran, G. Mantha, B. Srinivasan and U. P. N. Kannaian, *Energy Nexus*, 2023, **10**, 100197.
57 A. B. D. Nandiyanto, G. C. S. Girsang, R. Maryanti, R. Ragadhita, S. Anggraeni, F. M. Fauzi, P. Sakinah, A. P. Astuti, D. Usdiyana and M. Fiandini, *Commun. Sci. Technol.*, 2020, **5**, 31–39.
58 I. Langmuir, *J. Am. Chem. Soc.*, 1916, **38**, 2221–2295.
59 F. Okeola and E. Odebunmi, *Adv. Nat. Appl. Sci.*, 2010, 281–289.
60 R. A. Koble and T. E. Corrigan, *Ind. Eng. Chem.*, 1952, **44**, 383–387.
61 J. Wang and X. Guo, *Chemosphere*, 2020, **258**, 127279.
62 H. Freundlich, *Kapillarchemie, eine Darstellung der Chemie der Kolloide und verwandter Gebiete*, Akademische Verlagsgesellschaft, 1930.
63 R. Sips, *J. Chem. Phys.*, 1948, **16**, 490–495.
64 X.-L. Wu, P. Xiao, S. Zhong, K. Fang, H. Lin and J. Chen, *RSC Adv.*, 2017, **7**, 28145–28151.
65 J. Wang, M. Guan, Z. Qin, S. Zhang, J. Cheng and B. Xin, *Water*, 2025, **17**, 1630.
66 E. C. Lima, A. Hosseini-Bandegharaei, J. C. Moreno-Piraján and I. Anastopoulos, *J. Mol. Liq.*, 2019, **273**, 425–434.
67 F. Gritti and G. Guiochon, *Anal. Chem.*, 2006, **78**, 4642–4653.
68 E. M. A. Rahman, G. M. El-Subruiti, E. R. Atta and A. H. Moustafa, *ACS Omega*, 2025, **10**, 32680–32690.
69 K. M. Doke and E. M. Khan, *Rev. Environ. Sci. Bio/Technol.*, 2013, **12**, 25–44.
70 A. N. Ebelegi, N. Ayawei and D. Wankasi, *Open J. Phys. Chem.*, 2020, **10**, 166–182.
71 X. Jaramillo-Fierro and G. Cuenca, *Int. J. Mol. Sci.*, 2024, **25**, 4367.
72 Q. Wang, X. Lei, F. Pan, D. Xia, Y. Shang, W. Sun and W. Liu, *Colloids Surf., A*, 2018, **555**, 605–614.
73 A. Zaki, S. Rashad, M.-J. Lee and N. Shehata, *Mater. Adv.*, 2022, **3**, 8977–8988.
74 A.-L. Chang, B.-S. Nguyen, V.-H. Nguyen and C. Hu, *Mater. Chem. Phys.*, 2022, **276**, 125363.
75 Y. H. Kotp, *Environ. Sci. Pollut. Res.*, 2022, **29**, 81583–81608.
76 S. Mohanty and S. K. Maji, *Water Sci. Technol.*, 2020, **82**, 2562–2575.
77 S. Pysarenko, O. Kaminskyi, O. Chyhyrynets, R. Denysiuk and V. Chernenko, *Mater. Today: Proc.*, 2022, **62**, 7754–7758.
78 N. L. M. Tri, D. T. Thoa, N. H. Tri, N. M. Viet, T. T. V. Ha and N. C. Khoa, *Vietnam J. Chem.*, 2022, **60**, 708–717.
79 Y. Lin, J. Ma, W. Liu, Z. Li and K. He, *Environ. Sci. Pollut. Res.*, 2019, **26**, 10263–10273.
80 A. S. Mahadevi and G. N. Sastry, *Chem. Rev.*, 2013, **113**, 2100–2138.